Validation of the corrected Dang Van multiaxial fatigue criterion applied to turret bearings of FPSO offloading buoys

van Lieshout, Paula; den Besten, Henk; Kaminski, Mirek

DOI
10.1080/17445302.2016.1182461

Publication date
2017

Document Version
Accepted author manuscript

Published in
Ships and Offshore Structures

Validation of the corrected Dang Van multiaxial fatigue criterion applied to turret bearings of FPSO offloading buoys

P.S. van Lieshout[1], J.H. den Besten, M.L. Kaminski
[1]Department of Maritime and Transport Technology - Ship Hydromechanics & Structures
Delft University of Technology, The Netherlands

ABSTRACT

In engineering practice, multiaxial fatigue analyses are often avoided due to their complexity and computational intensity. However, damages have been encountered in turret bearings of FPSO offloading buoys which were likely caused by multiaxial fatigue. The Dang Van criterion has often been used to assess problems with multiaxial fatigue in rolling contacts. Therefore, this study set out to validate the application of the Dang Van criterion to turret bearings of FPSO offloading buoys. For this purpose, the criterion was corrected with a horizontal conservative locus for compressive hydrostatic stresses. Three load cases were identified based on the seakeeping analysis of an FPSO offloading buoy equipped with a wheel-rail turret bearing. For each load case, the surface pressure distribution and sub-surface stress states were determined analytically. Staircase tests were used to determine the characteristic parameters (α and β) of the Dang Van curve. Then, the Dang Van criterion was corrected and used to perform a multiaxial fatigue analysis in the critically stressed area of the wheel-rail contact. Finally, full scale long duration fatigue tests were used to validate the results. The corrected Dang Van criterion shows agreement with the experimental results and is not rejected as multiaxial fatigue criterion for application to turret bearings in FPSO offloading buoys.

Keywords: multiaxial fatigue, Dang Van criterion, turret bearing, rolling contact, wheel-rail

1 INTRODUCTION

Environmental and operational loads on ship and offshore structures may introduce a multiaxial stress state in certain components and structural details. Such multiaxial stress states can have a detrimental effect on the fatigue resistance and may result in premature fatigue damage (ISSC, 2012). For components and structural details experiencing predominantly uniaxial stress variations, generally accepted approaches have been developed which enable to make a fatigue lifetime estimation (e.g. IIW, Eurocode 3, DNVGL-RP-0005). However, when experiencing multiaxial stress variations additional complexity is introduced to the phenomenon of fatigue (Marquis & Socie, 2003; Papuga, 2011). Over the last decades a wide variety of methods and approaches have been developed specifically for multiaxial fatigue problems. However, validation often requires more investigation and experimental work. For the assessment of multiaxial fatigue in turret bearings, first steps in this direction have been taken by Lassen *et al.* (2012) who presented the fatigue design and a life prediction method for large roller bearings.

Multiaxial fatigue approaches are generally formulated on a macroscopic scale (i.e. a 'bulk' approach). However, there are also approaches which are formulated on a mesoscopic scale describing crack initiation and early crack growth on a granular level (Genet, 2006). Once yield is exceeded, grains in the crystal matrix can deform plastically as a consequence of cyclic loading. Under continuous accumulation of plastic strain fatigue crack initiation and early crack growth start to occur. Mesoscopic multiaxial fatigue criteria thus consider the amount of accumulated local plastic strain as driving fatigue parameter. A multiaxial fatigue damage theory was developed by Dang Van & Papadopoulos (1999) whereby the theory of shakedown is used to describe the behaviour of plastic flow on a granular level. The theorem defines three different stages of shakedown: elastic shakedown, plastic shakedown and ratchetting (Gannon *et al*., 2012; Zhang *et al.*, 2016). Elastic shakedown occurs when a particular material volume reverts into behaving elastically again after an initial plastic deformation. Plastic shakedown or ratchetting, on the other hand, cause an accumulation of plastic strain which will

eventually lead to the exceedance of ductility and thus crack initiation. It should be emphasized that the Dang Van criterion identifies whether crack initiation is likely to occur but cannot be used to obtain any information on fatigue lifetime.

The objective of this paper is to verify whether the Dang Van criterion is a valid criterion for the assessment of multiaxial fatigue in turret bearings of FPSO offloading buoys. This interest is driven by the fact that operators encountered premature fatigue damage after a service life of approximately seven years while the turrets were designed for a fatigue lifetime of twenty to twenty-five years. The Dang Van criterion could potentially be used to improve the multiaxial fatigue assessments of such turret bearings, but requires validation with experimental data. For this purpose, a wheel-rail turret bearing design was used which was specifically developed to improve the fatigue resistance. First, the rolling contact induced surface pressure distribution and sub-surface stresses were defined. Secondly, staircase tests were used to determine the fatigue resistance of the bearing material and to construct the Dang Van curve. This curve was corrected by a horizontal locus in the region of compressive hydrostatic stresses. Then, the Dang Van criterion was applied in the critically stressed region of the wheel-rail contact. Finally, the results were validated with full scale long duration fatigue tests and conclusions were drawn.

2 THEORETICAL BACKGROUND

2.1 Dang Van multiaxial fatigue criterion

Based on the principle of shakedown, the Dang Van criterion defines the fatigue damage parameter as the onset of accumulated mesoscopic plastic strain. A fatigue crack is thus assumed to initiate once the elastic shakedown limit is exceeded, meaning that the mesoscopic stresses exceed the elastic yield limit of the crystal, causing plastic flow. The Dang Van criterion formulates the mesoscopic state of stress σ as a subtraction of the macroscopic bulk stress Σ with a local residual stress which is a function of plastic mesoscopic strain ε_p (Ciavarella *et al.*, 2006). This relationship is given in Equation 1.

$$\sigma = \Sigma - f(\varepsilon_p) \tag{1}$$

However, the evaluation of the mesoscopic stress state based on the macroscopic one is not straightforward because different homogenization assumptions can be used (Hofmann *et al.*, 2009). An example of such a homogenization assumption is the Lin-Taylor homogenization assumption (see Equation 2), which considers strain equality at mesoscopic and macroscopic scale (Dang Van *et al.*, 1989; Dang Van, 2010). The sum of elastic and plastic mesoscopic strain (i.e. ε_e and ε_p) is presumed equal to the sum of elastic and plastic macroscopic strain (i.e. E_e and E_p).

$$\mathrm{E}_e + \mathrm{E}_p = \varepsilon_e + \varepsilon_p \tag{2}$$

For engineering practice the Dang Van criterion was reformulated using solely macroscopic stresses, making the assumption that elastic shakedown occurs both at mesoscopic and macroscopic level (Dang Van & Papadopoulos, 1999). The Dang Van criterion incorporates the maximum shear stress amplitude τ_a and the hydrostatic stress σ_H (see Equation 3-5) as functions of the principal stresses $\sigma_{1,2,3}$. It presumes the shear stress amplitude responsible for plastic gliding of slip bands (i.e. plastic straining) and the hydrostatic stress component for the mean stress effect (Desimone *et al.*, 2006). When the stress tensor is varying periodically with time, the Tresca yield criterion can be used to determine the shear stress component τ_a (Bernasconi *et al.*, 2006; Gayton & Lemaire, 2009). Equation 6 provides the Dang Van criterion as henceforth used in this paper. The relationship should be interpreted as an inclined line in the $\sigma_H - \tau_a$ plane with negative slope α and zero-crossing of the vertical axis at β. This is illustrated in Figure 1. For all data on or on the right side of the Dang Van curve fatigue crack initiation is expected.

$$max[\tau_a + \alpha\sigma_H] < \beta \tag{3}$$

$$whereby\ \tau_a = \frac{\sigma_1 - \sigma_3}{2};\ \sigma_H = \frac{\sigma_1 + \sigma_2 + \sigma_3}{3} \tag{4}$$

$$whereby\ \alpha = 3\left(\frac{\tau_{af,-1}}{\sigma_{af,-1}} - \frac{1}{2}\right);\ \beta = \tau_{af,-1} \tag{5}$$

$$\tau_{af,-1} = fatigue\ limit\ in\ fully\ reversed\ torsion$$
$$\sigma_{af,-1} = fatigue\ limit\ in\ fully\ reversed\ bending$$

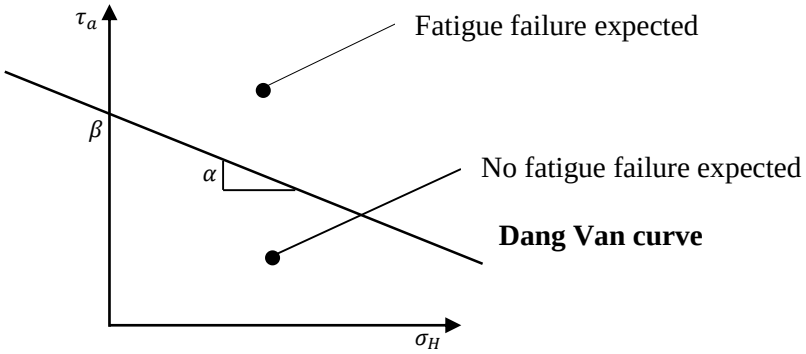

Figure 1: Illustration of the Dang Van curve representing the fatigue limit

2.2 Dang Van criterion applied to rolling contacts

In rolling contact problems compressive hydrostatic stresses are generated. Various researchers investigated the effect of such compressive hydrostatic stresses on the reliability of the Dang Van criterion (Desimone *et al.* 2006; Beretta & Foletti, 2011; Ciavarella & Monno, 2010). From these investigations it was concluded that the Dang Van criterion severely over-predicts the fatigue limit when compressive hydrostatic stresses are present, i.e. non-conservative.

From experimental tests Desimone *et al.* (2006) observed both elastic shakedown and rolling contact fatigue in the region of compressive hydrostatic stresses on the left side of the Dang Van curve (see Figure 2). Based on this observation, a horizontal projection was suggested as a conservative fatigue limit for the region of compressive hydrostatic stress values. The intersection of the locus was chosen such that the fatigue limit cannot become larger than the reversed plasticity limit. Desimone *et al.* (2005) and Beretta & Foletti (2011) calibrated the Dang Van criterion with experimental data from rolling contacts and confirmed that, for compressive hydrostatic stress values, the conservative horizontal locus shows a better fit than the Dang Van curve.

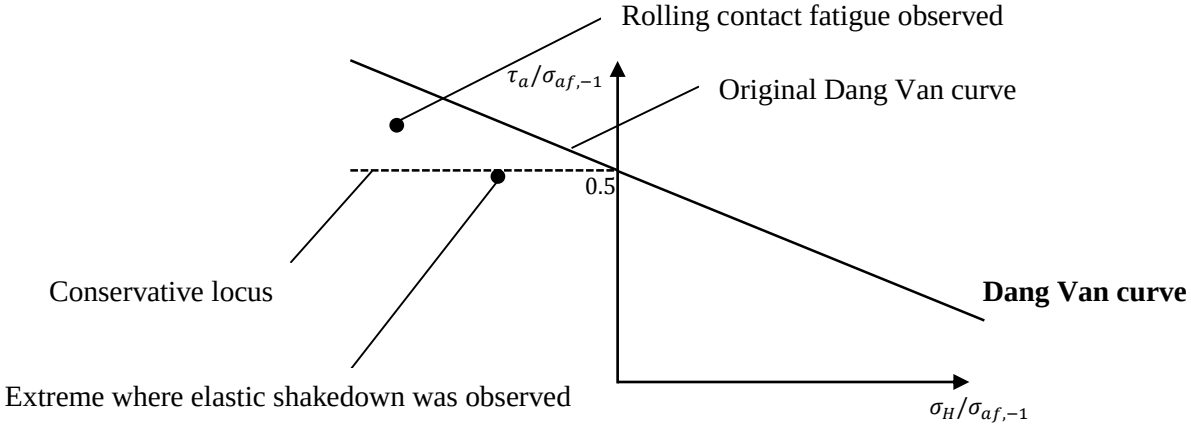

Figure 2: Illustration of the horizontal conservative locus which was developed by Desimone et al. (2005) for compressive hydrostatic stresses

3 VALIDATION

In various offshore applications a bearing facilitates the rotation of two individual parts with respect to each other (e.g. buoy, turrets, cranes). Conventional bearings for such applications are slewing bearings where three rings of rollers realize such relative rotations. NOV-APL has developed a new wheel-rail bearing design (Figure 3) where a segmented rail, clamped to one part, rotates with respect to another part with shaft connected radial wheels (in the horizontal plane) and axial wheels (in the vertical plane). The wheel shafts allow for a certain amount of bending in order to avoid the system being too rigid and to compensate for machining tolerances. Rail tracking is facilitated by conically shaped wheels with a double profile curvature. This geometry causes the turret to naturally rotate back to its centre position when a misalignment between traveling path of rail and wheels is induced. The rail consists of segments which are bolted to a supporting structure so that the operator can perform inspection or replacement when necessary. Based on the number of axial wheels, their diameter and the dimensions of the rail, it was concluded that the rail is the fatigue critical component. The rail is subjected to more than double the amount of load cycles on the axial wheels.

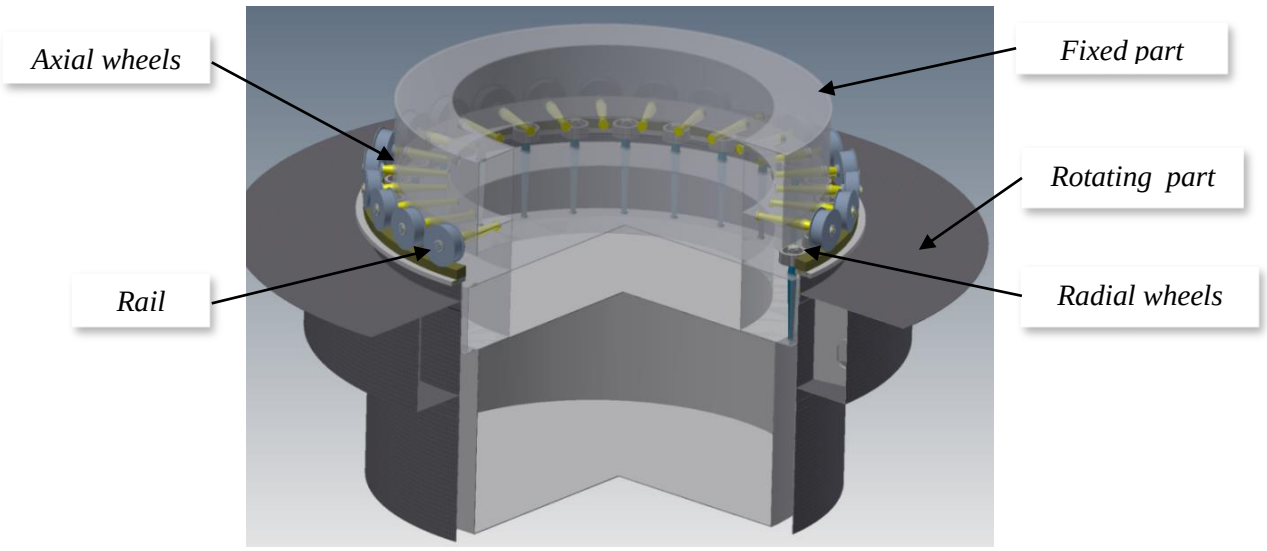

Figure3: Illustration of the wheel-rail bearing design which was considered throughout this validation study

3.1 Load case definition

Twelve load cases were identified from seakeeping analysis of a particular FPSO offloading buoy equipped with the wheel-rail bearing design. These load cases are listed in Table 1a. In the analysis environmental conditions (wind, waves and current) were taken into account as well as operational conditions (connection of offloading tanker) and filling of Oil Offloading Lines (OOL's) with water or oil. The mean vertical wheel loads that correspond with each load case are listed in Table 1b.

Load case	**Loading conditions**		
	Operational condition	***Environmental condition***	***Fill of OOL's***
1	Idle	Zero	Oil
2	Idle	Zero	Water
3	Idle	Low	Water
4	Idle	High	Water
5	Idle	Low	Oil
6	Tanker connected	Low	Oil
7	Idle	High	Oil
8	Tanker connected	High	Oil

9	Extreme loadings
10	Accidental load case 1 (line failure)
11	Accidental load case 2 (line failure)
12	Accidental load case 3 (compartment flooded)

Table 1a: Load cases identified from seakeeping analysis

Load case	1	2	3	4	5	6	7	8	9	10	11	12
Mean load [kN]	400	438	458	479	417	438	438	458	521	521	458	521

Table 1b: Mean vertical load on the axial wheel corresponding to each load case in Table 1a

Whilst in operation, the wheel-rail contact will be subjected to variable amplitude loading caused by changing environmental and operational conditions. This corresponds with variations in the endured load case. However, it was presumed that the encountered fatigue damage resulting from these loading conditions can be equated to a sequence of three static load cases. The conservative assumption of four daily rotations was used to determine the number of load cycles at each load level. A fatigue design lifetime of twenty-five years was considered which corresponds to a total of 876.000 load cycles. In Table 2 the three static load cases and their contribution to this total number of load cycles are listed.

Vertical load on wheel [kN]	**Number of load cycles [-]**
539	350.400
596	438.000
664	87.600

Table 2: Static load cases and their number of load cycles considered representative for a twenty-five year fatigue design lifetime

3.2 Surface and sub-surface stress analysis

As a first step towards validation of the corrected Dang Van criterion, the contact area, the maximum contact pressure and the sub-surface stress distribution in the considered wheel rail turret bearing have been determined.

Hertzian theory can make a reasonable approximation of the contact pressure distribution induced by a static contact between a round wheel and a flat surface under vertical compressive loading. However, the geometries of the rail and wheels in the bearing that are used in this validation study are more complex. The rail segment is sloped and the wheels have a conical shape with double profile curvature. Such complex geometries affect the dimensions of the elliptical contact area and the pressure distribution. However, Srivastava *et al.* (2013) developed an analytical approximation specifically for wheel-rail contacts in the railway industry where such additional parameters are taken into account (e.g. tapered wheel profile, wheel curvature). With this analytical approach the maximum surface pressure and the dimensions of the major and minor semi-axis of the elliptical presumed contact area were determined. The results are listed in Table 3.

Furthermore, the sub-surface stress distributions were determined using the analytical approach of Radzimovsky (1953) with reference to Figure 4 (see also Appendix A). Considering the most severe wheel load (i.e. 664 kN), Figure 5a shows the distribution of the sub-surface normal and shear stress components (i.e. $\sigma_x, \sigma_y, \sigma_z \; and \; \tau_{zx},$) along the rolling direction (i.e. the x-axis) at 4 mm surface depth. This surface depth was chosen because analysis of the sub-surface stress components along the centreline (i.e. the z-axis) showed that the shear stress component τ_{zx} reaches its maximum value here (see Figure 5c). Figure 5b shows the distribution of the other sub-surface normal stress components along the centreline.

Finally, the load path of the various stress components was plotted in the $\sigma - \tau$ plane in order to demonstrate the multiaxial behaviour. Such a plot is provided in Figure 6 considering the sub-surface stress distributions from Figures 5a-c.

Load case	Vertical load on wheel [kN]	Minor semi axis contact area [mm]	Major semi axis contact area [mm]	Maximum contact pressure [MPa]
1	539	7.5	46	747
2	596	7.8	47	773
3	664	8.1	49	801

Table 3: Results from the wheel-rail contact analysis considering the three load cases listed in Table 2

In the surface and sub-surface stress analysis dynamic effects of friction between the rolling bodies (leading to stick-slip), potential adhesion and surface roughness were not taken into account. However, horizontal forces on the buoy will induce counteracting friction force in the bushings of the bearing between its wheels and their shaft (i.e. along the y-axis). If the horizontal forces exceed the friction force, a relative motion between wheel and shaft is induced. However, if the horizontal force remains below the friction force a transverse shear will be induced in the wheel-rail contact area. Therefore, the friction coefficient between shaft and bushing was experimentally determined ($\mu = 0.1$) and used to account for an additional shear force in the stress tensor.

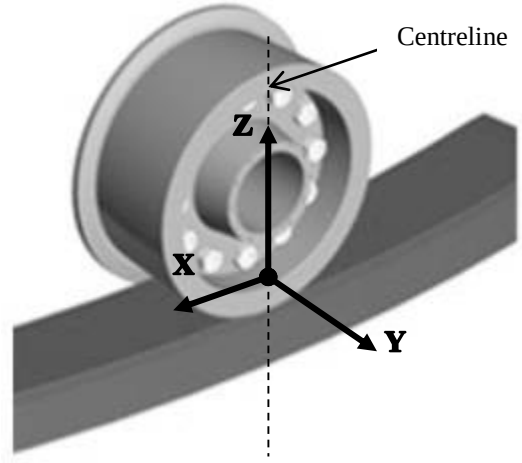

Figure 4: Schematic illustration of the used coordinate system in the wheel-rail contact area

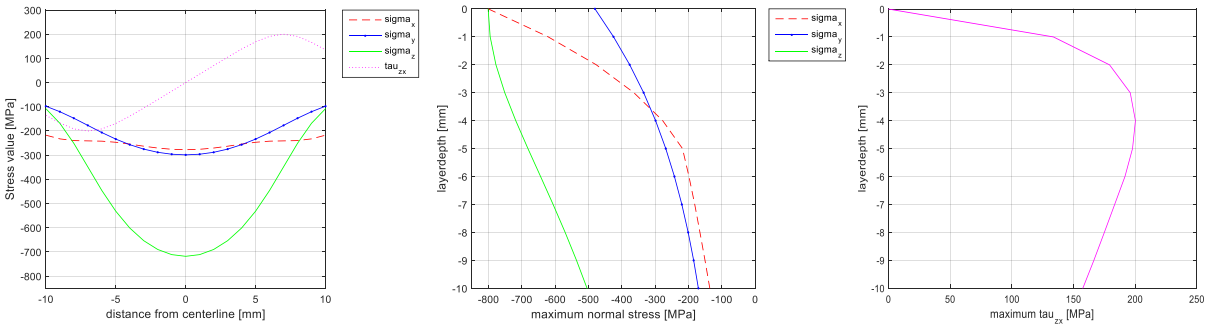

a **b** **c**

Figure 5: Sub-surface stress distributions in the elliptical contact wheel-rail contact area considering a vertical wheel load of 664 kN (a) Sub-surface stress distributions along the x-axis at 4mm depth (b) Sub-surface normal stress distributions along the centreline (c) Sub-surface shear stress distribution along the centreline

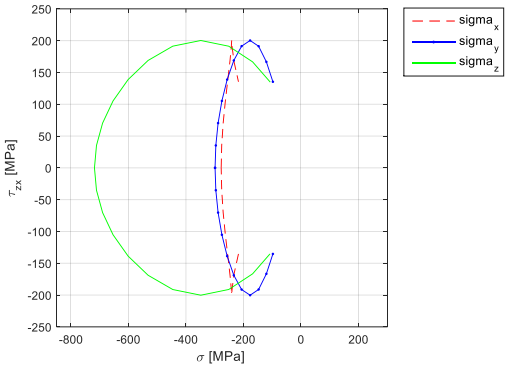

Figure 6: Load paths of the sub-surface stress components encountered with a vertical wheel load of 664 kN

3.4 Fatigue resistance

Small specimens were taken from the forged rail material (stainless martensitic steel) and were used for uniaxial fatigue testing following a conventional staircase test as described in ISO 12107. The specimens were sampled from a 40 mm thick plate which was cut from a testing block (750 x 380 x 320 mm). The samples were taken perpendicular to the forging direction because elongation of inclusions in the forging direction can cause anisotropic fatigue behaviour (Pessard *et al.*, 2012). By transverse sampling this will not influence the fatigue behaviour of the specimens. From the first batch, sixteen specimens were sampled and twelve of these specimens were tested at a load ratio (i.e. R-ratio) of 0.05. In a second batch, another four specimens were sampled from the surface. Also a third batch of samples was made providing six samples. For the tests at an R-ratio of -1 the remaining four specimens from the first batch, two specimens from the second batch and two specimens from a third batch were used. The remaining two specimens from the second batch lead to unusable results. The remaining four specimens from the third batch were used for tensile testing. Each of these specimens were taken from a different surface area of the testing block. With these tensile tests it was investigated whether the yield strength of the steel is affected by its orientation during quenching. This appeared not to be the case. The results from the staircase tests are listed in Table 4 and 5.

The staircase tests were performed with R-ratios of $R = 0.05$ and $R = -1$ under sinusoidal loading. The dimension of the specimens were in accordance with ISO 12107 as depicted in Figure 7. Two classical staircase tests were performed, defining run-outs at exceedance of $1 \cdot 10^7$ cycles. A high frequency pulsator was used with an approximate frequency of 200 Hz. The starting value and step size of the staircase test with $R = -1$ were slightly higher than the starting value of the staircase with $R = 0.05$. In Figure 8 a picture is shown of the test specimen in the testing machine during fatigue testing.

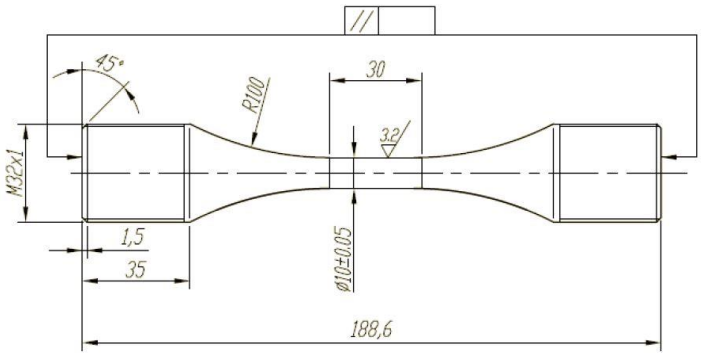

Figure 7: Dimensions of the small scale test specimen according to ISO 12107

Figure 8: Small scale test specimen during fatigue testing

From the small scale test results, the mean value (μ) and standard deviation (SD) of the materials fatigue limit were obtained with the Dixon-Mood method (see Table 6). More detailed information on the calculation procedures behind this method can be found in reference (Dixon & Mood, 1948). This method is comprehensive and enables to obtain a fairly accurate estimate of the mean value (corresponding to the fatigue limit) provided a limited amount of data (Pollak, 2005). However, the standard deviation is generally very inaccurate for relatively small data sets. This is caused by the very nature of staircase testing itself which concentrates all the data around the mean (Pollak, 2005). Therefore, the standard deviation was henceforth excluded from the analysis. This was justified due to the fact that the analytical and experimental results were used in a comparison. In both cases the mean value was used instead of the design value (i.e. mean minus two times standard deviation).

Staircase test 1: $R = 0.05$ **Starting value = 480 MPa** **Stepsize = 20 MPa** **0 = Run-out** **X = Failure**												
Specimen	1	2	3	4	5	6	7	8	9	10	11	12
Batch	1	1	1	1	1	1	1	1	1	1	1	1
Stress range [MPa]												
500		X								X		X
480	0		X						0		0	
460				X				0				
440					X		0					
420						0						
Number of cycles	2 $\cdot 10^7$	1.07 $\cdot 10^6$	2.52 $\cdot 10^6$	5.34 $\cdot 10^6$	1.86 $\cdot 10^6$	1.41 $\cdot 10^7$	2 $\cdot 10^7$	2 $\cdot 10^7$	2 $\cdot 10^7$	9.03 $\cdot 10^6$	1.79 $\cdot 10^7$	1.46 $\cdot 10^6$

Table 4: Staircase test results using load ratio $R = 0.05$

Staircase test 2: $R = -1$ **Starting value = 580 MPa** **Stepsize = 30 MPa** **0 = Run-out** **X = Failure**								
Specimen	13	14	1	2	3	4	1	2
Batch	1	1	2	2	2	2	3	3
Stress range [MPa]								
610								X
580	X						0	
550		X				0		
520			X		0			
490				0				
Number of cycles	5.42 $\cdot 10^6$	2.49 $\cdot 10^6$	1.89 $\cdot 10^6$	2 $\cdot 10^7$	2 $\cdot 10^7$	2 $\cdot 10^7$	2 $\cdot 10^7$	6.40 $\cdot 10^6$

Table 5: Staircase test results using load ratio $R = -1$

Staircase test	***Mean stress range $\Delta\sigma_\mu$ [MPa]***	***Standard Deviation SD [MPa]***
1: $R = -1$	470	44
2: $R = 0$	550	111

Table 6: Results from analysing the staircase test data using the Dixon-Mood method

The staircase test results ensued into a mean stress range (obtained with the Dixon-Mood method) for each load ratio ($R = -1$ and $R = 0.05$). Harmonic sinusoidal loading was used during staircase testing. Therefore, Equations 6-9 could be formulated and used to obtain the maximum hydrostatic stress and the maximum shear stress amplitude from these mean stress ranges. The results are listed in Table 7. The Dang Van curve could now be determined by plotting the data points corresponding to the two sets of values for hydrostatic stress and shear stress amplitude (i.e. data point p_1 with coordinates $(\sigma_{H,R=-1},\ \tau_{a,R=-1})$ and data point p_2 with coordinates $(\sigma_{H,R=0.05}, \tau_{a,R=0.05})$). With a linear fit between these two data points the Dang Van curve was then determined as illustrated in Figure 9. The corresponding characteristic Dang Van parameters are $\alpha = 0.34$ and $\beta = 170$.

$$\sigma_{H,R=0.05} = \max\left(\frac{\Delta\sigma_\mu/2}{3} + \frac{\Delta\sigma_\mu/2}{3}\sin(\omega t)\right) \tag{6}$$

$$\sigma_{H,R=-1} = max\left(\frac{\Delta\sigma_\mu/2}{3}\ \sin(\omega t)\right) \tag{7}$$

$$\tau_{a,R=0.05} = max\left(\frac{\Delta\sigma_\mu/2}{2}\sin(\omega t)\right) \tag{8}$$

$$\tau_{a,R=-1} = max\left(\frac{\Delta\sigma_\mu/2}{2}\sin(\omega t)\ \right) \tag{9}$$

Staircase test	***Maximum hydrostatic stress σ_H [MPa]***	***Maximum shear stress amplitude τ_a [MPa]***
1: $R = -1$	157	118
2: $R = 0$	92	138

Table 7: Data points for determination of the Dang Van curve extracted from the staircase test results

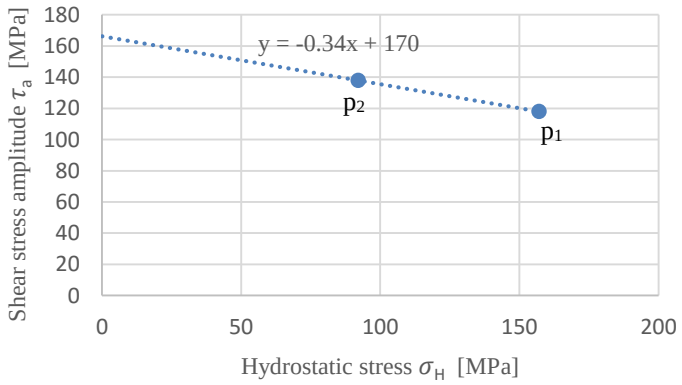

Figure 9: Dang Van Curve determined from staircase test results

3.5 Results of the Dang Van Criterion

For each load cycle a most critical point can be identified in the contact region. At this critical location the hydrostatic stress and shear stress amplitude correspond to a data point in the Dang Van diagram which lies closest to the Dang Van curve. When this point lies on or on the right side of this curve it is foreseen that fatigue crack initiation occurs.

The objective of this paper was to validate the corrected Dang Van criterion considering the previously discussed wheel-rail bearing. Therefore, two steps were undertaken. First the local stress

tensor in the contact region of the wheel-rail contact was determined. With this tensor the hydrostatic stress and shear stress amplitude were determined in the critically stressed area at incremental locations of 1 mm along the x- and z axis in a region of $20mm\ x\ 10\ mm$ (see Figure 10). In total 441 data points were analysed and the most severe wheel load of $664\ kN$ was considered. Secondly, the Dang Van curve which resulted from staircase testing (Figure 9) was corrected by a horizontal locus for the region of compressive hydrostatic stresses. This was done in coherence with the conservative locus proposed by Desimone *et al.* (2006) which intersects the normalized vertical axis at $\tau_a/\sigma_{af,-1} = 0.5$ (see Section 2.2). For this purpose, the expression for α (given in Equation 5) was rewritten so that the fatigue limit in fully reversed bending (i.e. $\sigma_{af,-1}$) could be expressed by Equation 10. This result was used to determine the value of the shear stress amplitude where the conservative locus intersects the vertical axis of the Dang Van diagram (generated in previous Section). The intersection occurs at $\tau_a = 138\ MPa$. Figure 11 shows the data points corresponding to the stress states in the analysed most critically stressed area in the Dang Van diagram. In this figure the experimentally determined Dang Van curve and the considered conservative locus were also depicted.

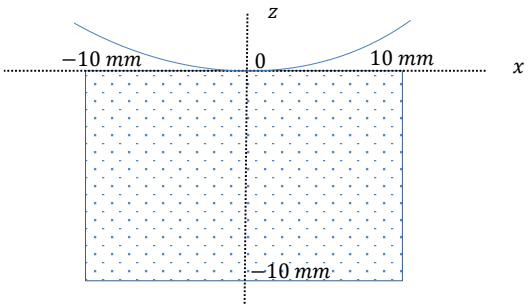

Figure 10: Illustration of the analysed contact area in the wheel-rail bearing design

$$\sigma_{af,-1} = \frac{\tau_{af,-1}}{\frac{\alpha}{3}+\frac{1}{2}} \qquad (10)$$

$$whereby\ \tau_{af,-1} = \beta$$

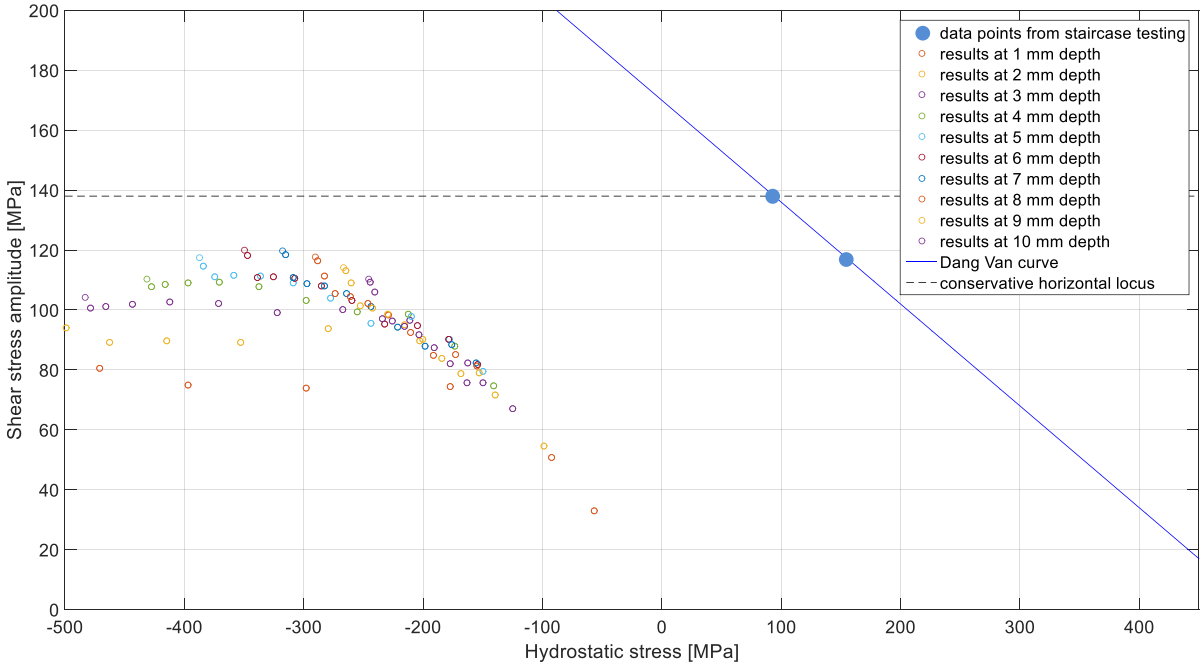

Figure 11: Analytical results from analysing the most critically stressed region in the wheel-rail contact plotted in the Dang Van diagram including the experimentally determined Dang Van curve and conservative horizontal locus

3.6 Results from experimental testing

In order to validate the results, experimental long duration tests were executed at the load levels listed in Table 2. For this purpose a full scale test setup of the wheel-rail rolling contact was designed and constructed by NOV-APL. The test rig consisted of a pendulum frame with two mirrored rail sections which were able to rotate around the z-axis (rotation in the horizontal plane). These angular rotations were induced by a hydraulic cylinder that was connected to the test rig on one side, and to the outer end of the pendulum frame on the other side. The motion of the pendulum frame was smoothened by a sinusoidal speed control on the hydraulic cylinder. On both sides of the pendulum frame the rail sections were in contact with an axial wheel which was connected to the test rig via a shaft. Three different vertical compressive loads were applied sequentially (Table 2) on both wheels by pressurising a jacket which was located between the tension frame and the upper wheel shaft. In Figure 12 a schematic illustration of the test rig is provided. The results of the experimental long duration tests are listed in Table 8.

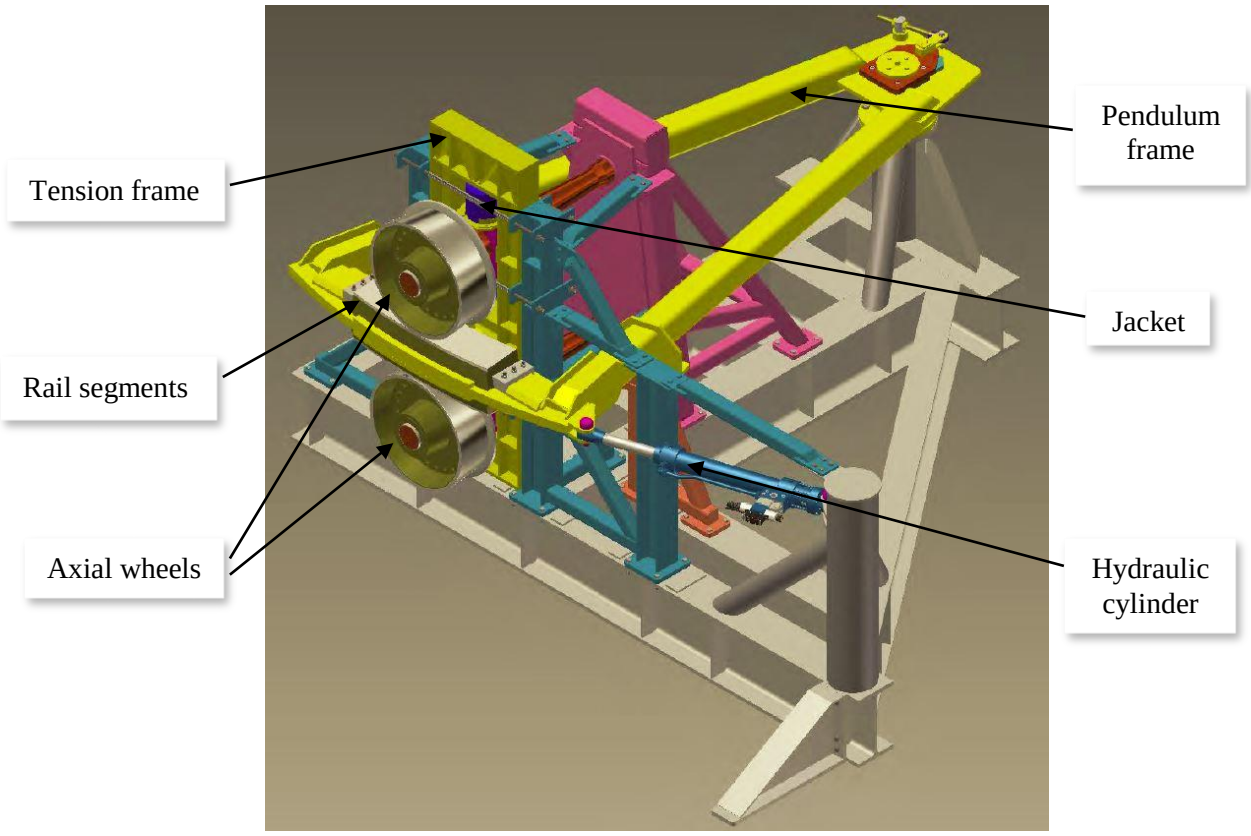

Figure 12: Test rig for full scale long duration fatigue testing indicating the main components

Vertical load on wheel [kN]	Number of load cycles [-]	Crack initiation in wheel-rail contact observed?
539	350.400	No
596	438.000	No
664	87.600	No

Table 8: Results from experimental long duration fatigue testing

4 DISCUSSION AND CONCLUSION

Analytical and experimental work was executed in order to validate the application of the corrected Dang Van criterion in the considered wheel-rail turret bearing. The stress state in the most critically stressed contact region was determined and compared to the Dang Van curve generated with experimental data from two staircase tests. A correction to the Dang Van curve was applied in the region of compressive hydrostatic stresses resulting in a conservative horizontal locus. The analytically determined hydrostatic stresses and shear stress amplitudes in the wheel-rail contact region (based on the macroscopic stress tensor) do not indicate fatigue crack initiation for the most severe wheel load of $664\ kN$. The data points corresponding to the stress values remain on the left side of the Dang Van curve and below the conservative locus. Two other static load cases were considered for the representation of a twenty-five year fatigue lifetime. However, because the highest load case is considered governing crack initiation is neither expected at these two load levels.

Furthermore, experimental long duration fatigue tests were performed whereby the wheel-rail contact was exposed to three static load levels. These load levels and the number of load cycles were considered representative for a fatigue lifetime of twenty-five years. After completion of the tests no fatigue crack initiations were observed. This finding is in agreement with the analytically obtained results from application of the corrected Dang Van criterion. When the engineering formulation of the Dang Van criterion is corrected with a horizontal locus for compressive hydrostatic stresses (as suggested by Desimone *et al.* (2006)) it appears to be still a valid multiaxial fatigue criterion for turret bearings of FPSO offloading buoys.

ACKNOWLEDGEMENTS

The authors gratefully acknowledges the support for this work by NOV-APL, TOTAL S.A. and Delft University of Technology. Furthermore, they wish to thank NOV-APL and TOTAL S.A. for their kind permission to use the data from small scale fatigue testing, full scale long duration fatigue testing and the seakeeping analysis.

REFERENCES

Beretta, S., & Foletti, S. (2011). Propagation of small cracks under RCF: a challenge to Multiaxial Fatigue Criteria. *Politecnico di Milano*.

Bernasconi, A., Davoli, P., Filippini, M., & Foletti, M. (2005). An integrated approach to rolling contact sub-surface fatigue assessment of railway wheels. *Wear*, 973-980.

Bernasconi, A., Filippini, M., Foletti, S., & Vaudo, D. (2006). Multiaxial fatigue of a railway wheel steel under non-proportional loading. *International Journal of Fatigue 28*, 663-672.

Charkaluk, E., Constantinescu, A., Maitournam, H., & Dang Van, K. (2009). Revisiting the Dang Van criterion. *Procedia Engineering 1*, 143-146.

Ciavarella, M., & Monno, F. (2010). A comparison of multiaxial fatigue criteria as applied to rolling contact fatigue. *Tribology International 43*, 2139-2144.

Ciavarella, M., Monno, F., & Demelio, G. (2006). On the Dang Van fatigue limit in rolling contact fatigue. *International Journal of Fatigue 28*, 852-863.

Dang Van, K. (2010). On a unified fatigue modelling for structural analysis based on the shakedown concept. *Palaiseau, France: Ecole Polytechnique*.

Dang Van, K., & Papadopoulos, I. V. (1999). *High cycle metal fatigue - From theory to applications No. 392.* CISM couses and lecures - International Centre for Mechanical Sciences.

Dang Van, K., Griveau, B., & Message, O. (1989). On a new multiaxial fatigue limit criterion: Theory and application. *Biaxial and Multiaxial Fatigue*, 479-496.

Desimone, H., Bernasconi, A., & Beretta, S. (2006). On the application of Dang Van criterion to rolling contact fatigue. *Wear 260*, 567-572.

Dixon, W. J., & Mood, A. M. (1948). A method for obtaining and analyzing sensitivity data. *Journal of the American Statistical Association 43*, 109-126.

Ekberg, A. (1999). *Rolling contact fatigue of railway wheels.* Sweden: Department of Solid Mechanics - Chalmers University of Technology.

Fojtík, F. (2011). Appication of selected fatigue criteria on the results of multiaxial high-cycle fatigue experiments. *Modelling of mechanical and mechatronic systems 4th International conference*, (pp. 104-111). Slovak Republic.

Gannon, L. G., Pegg, N. G., Smith, M. J., & Liu, Y. (2012). Effect of residual stress shakedown on stiffened plate strength and behaviour. *Ship and Offshore Structures Vol. 8*, 638-652.

Gayton, N., & Lemaire, M. (2009). Reliability assessment of structures subjected to fatigue failure. *Ship and Offshore Structures Vol. 4*, 229-239.

Genet, G. (2006). *A statistical approach to multi-input equivalent fatigue loads for the durability of automotive structures.* Sweden: Chalmers University of Technology/Goteborg University - Department of Mathematical Sciences.

Hofmann, F., Bertolino, G., Constantinescu, A., & Ferjani, M. (2009). Numerical exploration of the Dang van High Cycle Fatigue Criterion. *Journal of Mechanics of Materials and Structures 2*, 293-308.

ISSC. (2012). *Fatigue and Fracture.* Rostock, Germany: 18th International ship and offshore structures congress.

Jiang, Y. (2000). A fatigue criterion for general multiaxial loading. *Fatigue and Fracture of Engineering Materials and Structures 23*, 19-23.

Lassen, T., Hansen, S. E., & Askestad, S. (2012). Fatigue design of roller bearing for large FPSO turrets. *31th International Conference on Ocean Offshore and Arctic Engineering.* Rio de Janeiro, Brasil.

Marquis, G. B., & Socie, D. F. (2003). *Comprehensive Structural Integrity - Cyclic loading and Fatigue.* Elsevier.

Morel, F. (2000). A critical plane approach for life prediction of high cycle fatigue under multiaxial variable amplitude loading. *Internation Journal of Fatigue 22*, 101-119.

Papadopoulos, I. V. (1998). Critical plane approaches in high-cycle fatigue: on the definition of the amplitude and mean value of the shear stress acting on the critical plane. *Fatigue and Fracture of Engineering Materials and Structures 21*, 269-285.

Papuga, J. (2011). A survey on evaluating the fatigue limit under multiaxial loading. *International Journal of Fatigue 33*, 153-165.

Pascual, F. G., & Meeker, W. Q. (1999). Estimating fatigue curves with the Random Fatigue-Limit Model. *Technometrics 41*, 277-289.

Peridas, G., Korsunsky, A. M., & Hills, D. A. (2003). The relationship between the Dang Van criterion and the traditional bulk fatigue criteria. *Journal of Strain Analysis Vol. 38 No. 3*, 201-206.

Pessard, E., Morel, F., Bellett, D., & Morel, A. (2012). A new approach to model the fatigue anisotropy due to non-metallic inclusions in forged steels. *International Journal of Fatigue*, 168-178.

Pollak, R. D. (2005). *Analysis of methods for determining high cycle fatigue strength of a material with investigation of Ti-6Al-4V Gigacycle fatigue behaviour.* Ohio: Air Force institute of technology.

Radzimovsky, E. I. (1953). *Stress distribution and strength condition of two rolling cylinders pressed together.* Urbana: University of Illinois.

Srivastava, J. P., Sarkar, P. K., & Ranjan, V. (2013). An approximate analysis for Hertzian elliptical wheel-rail contact problem. *1st International and 16th National Conference on Machines and Mechanicms*, (pp. 249-253). India.

Zhang, X., Paik, J. K., & Jones, N. (2016). A new method for assessing the shakedown limit state associated with the breakage of a ship's hull girder. *Ship and Offshore Structures Vol. 11*, 92-104.

APPENDIX A

An analytical method, based on the rolling contact of two compressed cylinders, was used to determine the sub-surface stress components in the wheel-rail contact area. This method presumes an intersection over the width of the elliptical contact area, considering q as the load per unit length and the width of the elliptical contact area by its minor semi-axis a (see Figure A1).

$$q = \int_{-a}^{a} P_0 \sqrt{1 - \frac{x^2}{a^2}}\, dx \tag{A.1}$$

Each stress component was determined as a function of the elliptic coordinates φ and θ, q, a and Lame's constants μ and λ (which are a function of the E-modulus E and Poisson's ratio ν). The directionality of the stress components was defined in accordance with the coordinate system of Figure 4.

$$\sigma_x = -\frac{2q}{\pi a} e^{-\varphi} sin(\theta) + \frac{2q}{\pi a} sin(\theta) sinh(\varphi) \left(1 - \frac{sinh(2\varphi)}{cosh(2\varphi) - cos(2\theta)}\right) \tag{A.2}$$

$$\sigma_y = -\frac{2q}{\pi a} \cdot \frac{\lambda}{\lambda + \mu} e^{-\varphi} sin(\theta) \tag{A.3}$$

$$\sigma_z = -\frac{2q}{\pi a} e^{-\varphi} sin(\theta) - \frac{2q}{\pi a} sin(\theta) sinh(\varphi) \left(1 - \frac{sinh(2\varphi)}{cosh(2\varphi) - cos(2\theta)}\right) \tag{A.4}$$

$$\tau_{xy} = 0 \tag{A.5}$$

$$\tau_{xz} = -\frac{2q}{\pi a} \sinh(\varphi) \sin(\theta) \frac{\sin(2\theta)}{\cosh(2\varphi) - \cos(2\theta)} \tag{A.6}$$

$$\tau_{yz} = 0 \tag{A.7}$$

$$\mu = \frac{E}{(2(1+\nu)} \tag{A.8}$$

$$\lambda = \frac{\nu E}{(1+\nu)(1-2\nu)} \tag{A.9}$$

All other terms in the Equations A.2-A.6 can be expressed by φ and θ which can be derived from Equations A.10 and A.11.

$$\sinh(\varphi) = \pm \sqrt{\frac{-(a^2 - x^2 - z^2) + \sqrt{(a^2 - x^2 - z^2)^2 + 4a^2 z^2}}{2a^2}} \tag{A.10}$$

$$\sin(\theta) = \pm \sqrt{\frac{(a^2 - x^2 - z^2) + \sqrt{(a^2 - x^2 - z^2)^2 + 4a^2 z^2}}{2a^2}} \tag{A.11}$$

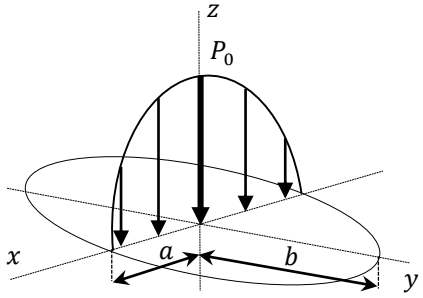

Figure A1: Schematic illustration of the load distribution per unit length in an elliptically shaped contact region